

A Fixed Switching Frequency Direct Model Predictive Control for Grid-Tied Converters with *LCL* Filters under Adverse Grid Conditions

Qifan Yang, Petros Karamanakos, *Senior Member, IEEE*,

Wei Tian, *Member, IEEE*, Tobias Geyer, *Fellow, IEEE*,

Ralph Kennel, *Senior Member, IEEE*, and Marcelo Lobo Heldwein, *Senior Member, IEEE*

Abstract—This article presents a direct model predictive control (MPC) scheme for grid-tied converters (GTCs) with *LCL* filters operating under nominal and adverse grid conditions. Specifically, the proposed MPC algorithm achieves a high-quality grid current in steady state and fast dynamic responses that characterize direct controllers due to the absence of a dedicated modulator. Thanks to the adopted modeling approach, the control and modulation problems are formulated together as a multiple-input multiple-output (MIMO) problem. In doing so, not only the controller design process is greatly simplified, but also favorable performance in terms of controller bandwidth and robustness is achieved. This is in stark contrast to conventional linear control methods, where the existence of different cascaded and/or parallel control loops oftentimes leads to an adverse interaction with each other. Consequently, as also demonstrated with the presented experimental results, the proposed algorithm achieves superior performance for a wide range of operating conditions, rendering it as a promising control approach for the systems in question.

Index Terms—Model predictive control (MPC), direct control, multiple-input multiple-output (MIMO) systems, power electronic systems.

I. INTRODUCTION

DISTRIBUTED power-generation systems using renewable energy sources are experiencing significant growth worldwide [1]. Grid-tied converters (GTCs) are the critical technology to integrate different renewable energy sources into the grid in an efficient and flexible manner [2]. Considering the power quality and stability of power networks, stringent requirements are imposed on GTCs during nominal as well as faulty grid conditions. More specifically, during nominal operation, the harmonics of the current/voltage injected into the point of common coupling (PCC) are tightly limited by harmonic grid codes, such as the IEEE 519 [3] and the IEC 6100-2-4 [4] standards. As for faulty grid conditions, the power converters should be able to stay connected to the grid and maintain continuous operation throughout a (short) period of faults.

Q. Yang, W. Tian, R. Kennel and M. L. Heldwein are with the Chair of High-Power Converter Systems, Technical University of Munich, 80333 Munich, Germany; e-mail: qifan.yang@tum.de, wei.tian@tum.de, raphael.kennel@tum.de, marcelo.heldwein@tum.de

P. Karamanakos is with the Faculty of Information Technology and Communication Sciences, Tampere University, 33101 Tampere, Finland; e-mail: p.karamanakos@ieee.org

T. Geyer is with ABB Systems Drives, 5300 Turgi, Switzerland; e-mail: t.geyer@ieee.org

To meet the limits on the amplitude of grid current harmonics and the total harmonic distortion (THD), *LCL* filters are often used with GTCs since they significantly attenuate the switching harmonics [5]. However, the presence of an *LCL* filter complicates the controller design because the resulting higher-order system has a pair of resonant poles located at the stability boundary [6]. Conventionally, this challenge is addressed by designing the current controller in the synchronous reference frame—thus enabling the use of proportional-integral (PI) controllers—and augmenting it with an active damping loop [7]. The latter most commonly relies on the filter capacitor current feedback [8]–[10]. Nonetheless, tuning the parameters of the active damping and current control loops is a non-trivial task [8], while the system can even become unstable when the *LCL* filter resonance frequency is at or near to one-sixth of the sampling frequency [9]. Moreover, in case low-order grid harmonics—mainly the 5th and 7th—are present, then dedicated controllers are required to eliminate them as they cannot be mitigated by the filter. To this aim, PI controllers can be employed that are designed in different reference frames that rotate at the angular frequency of the harmonics in question. Alternatively, proportional-resonant (PR) controllers tuned to resonate at the harmonic frequencies can be used [1]. Either way, the existence of additional control loops renders the tuning procedure even more cumbersome.

Moreover, during grid faults, imbalanced grid voltages appear at the PCC that include both the positive- and negative-sequence voltage components [11]. An intuitive control approach under such grid conditions is to design two control loops in reference frames that rotate in synchronism with these components [12]. By doing so, both the positive- and negative-sequence components of the grid current can be controlled and the (instantaneous) active/reactive power at the PCC can be regulated. However, the positive- and negative-sequence components of the current cannot be fully decoupled, especially during transients. As shown in [12], notch filters (NFs) can be used to attenuate the interaction between the two current components. This, however, significantly reduces the controller bandwidth and it can cause stability issues when the damping factor of the NF is not properly tuned [2].

An alternative control approach for GTCs with *LCL* filters is model predictive control (MPC) as it particularly suitable for multiple-input multiple-output (MIMO) and high-order systems [13]. The most popular MPC method is direct MPC with

reference tracking, also known as finite control set MPC (FCS-MPC), due to its intuitive concept [14]. However, FCS-MPC lacks a modulation stage, thus resulting in a variable switching frequency and, consequently, spread current harmonic spectra [15]–[17]. Such a feature is undesirable when GTCs are of interest since the spread low-frequency harmonics cannot be effectively mitigated, meaning that the relevant harmonic grid standards may be violated. Therefore, indirect MPC, i.e., MPC with a dedicated modulation stage, such as carrier-based pulse width modulation (CB-PWM) or space vector modulation (SVM) [18], seems to be a better MPC-based derivative for GTCs [19]–[21]. Indirect MPC methods are most commonly formulated as a quadratic program (QP), which can be easily solved either analytically or numerically with the help of off-the-shelf solvers. However, the method in [19] is prone to suboptimality, and thus inferior performance, as the indirect MPC problem is formulated as an unconstrained QP. On the other hand, [20] imposes constraints on the modulating signal that is fed into the modulator, but it considers only nominal grid conditions, thus failing to demonstrate the full potential of MPC. In contrast to this, [21] accounts for grid faulty conditions, albeit only under symmetrical faults. Therefore, more challenging operating conditions, such as asymmetrical grid faults where significant negative-sequence components appear in the grid voltage, are not addressed.

Regardless of the problem considered, the dynamics of indirect MPC are typically slower from those of direct control methods as they are limited by the modulator. To exploit the fast dynamics of direct MPC while tackling the problems of variable switching frequency and spread harmonic spectra, some direct MPC with precomputed switching sequences have been proposed [22]–[24]. These methods employ switching patterns akin to those of CB-PWM/SVM, and calculate the optimal switching time instants or duty cycles for each voltage vector. However, the optimization problem in [22] is designed as an unconstrained one, thus exhibiting the disadvantages of such a formulation, as mentioned above. As for [23], the constrained optimization problem therein cannot guarantee that the ripple of the sampled variables does not enter the control loop. Consequently, undesired low-frequency harmonics result which contribute to a higher THD. These issues are effectively addressed in [24] by designing the objective function of the MPC problem to capture the approximate rms value of the output ripple and more heavily penalize the reference tracking error at the sampling instants. However, [24] assumes a strong grid and nominal operating conditions, i.e., operation under challenging operating conditions is not considered.

Motivated by the above, this work extends the MPC method in [24] to control GTCs with *LCL* filters under adverse grid conditions. To this aim, a prediction model suitable for a wide range of operating conditions, including persistent disturbances—such as grid voltage harmonics—and unsymmetrical grid faults, is first derived. Subsequently, the control and modulation problems are designed as one computational entity in the form of a constrained QP. As a result, this direct control structure allows for not only favorable steady-state operation, but also superior dynamic performance. Such a behavior is further enabled by the MIMO structure of the

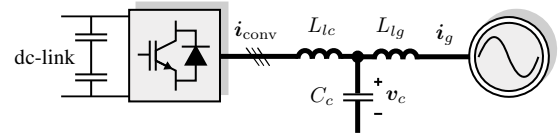


Fig. 1: Grid-tied converter with an *LCL* filter.

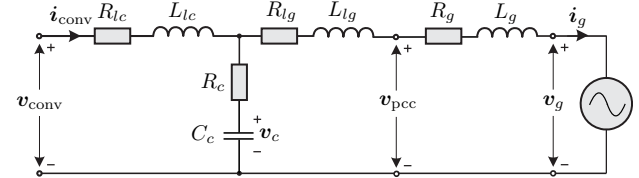


Fig. 2: Equivalent circuit of the grid-tied converter with an *LCL* filter.

MPC algorithm as the adverse interaction between multiple control loops—which often causes oscillations during transients, or even stability issues in critical operating conditions, especially when the parameters are not properly tuned—is altogether avoided. Note that this superior performance is achieved without requiring to change the control structure or the controller parameters depending on the grid conditions, which is in stark contrast to conventional linear control schemes. Finally, to clearly demonstrate the advantages of the proposed control scheme, a comprehensive experimental study is presented along with a comparison with the conventional PI-based voltage-oriented control (VOC).

This article is structured as follows. Section II introduces the mathematical model of the GTC with an *LCL* filter suitable for nominal and adverse grid conditions. The direct MPC scheme is described and formulated in Section III. Following, its performance is experimentally verified and compared with the conventional control methods in Section IV. Finally, Section V concludes the paper.

II. MATHEMATICAL MODEL OF THE SYSTEM

Fig. 1 depicts the GTC with an *LCL* filter. The system is modeled in the stationary orthogonal $\alpha\beta$ frame, and thus, any variable $\xi_{abc} = [\xi_a \ \xi_b \ \xi_c]^T$ in the abc -plane is mapped into a variable $\xi_{\alpha\beta} = [\xi_\alpha \ \xi_\beta]^T$ in the $\alpha\beta$ -plane via $\xi_{\alpha\beta} = K\xi_{abc}$,¹ where

$$K = \frac{2}{3} \begin{bmatrix} 1 & -\frac{1}{2} & -\frac{1}{2} \\ 0 & \frac{\sqrt{3}}{2} & -\frac{\sqrt{3}}{2} \end{bmatrix}.$$

A three-phase two-level voltage source inverter (VSI) is considered in this work. Since the phase voltage can assume two discrete values, i.e., $-\frac{V_{dc}}{2}$ and $\frac{V_{dc}}{2}$, with V_{dc} denoting the dc-link voltage, the single-phase switch position can be modeled by the integer variable $u_x \in \{-1, 1\}$, with $x \in \{a, b, c\}$. Therefore, by introducing the three-phase switch position $u_{abc} = [u_a \ u_b \ u_c]^T$, the converter output voltage v_{conv} is given by

$$v_{conv} = \frac{V_{dc}}{2} Ku_{abc}. \quad (1)$$

Fig. 2 shows the equivalent circuit of the system, where v_{conv} (v_g) and i_{conv} (i_g) are the converter (grid) voltage and

¹In the sequel of the paper, the subscript $\alpha\beta$ used to denote variables in the $\alpha\beta$ -plane is omitted to simplify the notation. Variables in the abc -plane are indicated with the corresponding subscript.

current, receptively, and \mathbf{v}_c is the voltage across the filter capacitor. Besides, L_{lc} (L_{lg}) and R_{lc} (R_{lg}) are the converter (grid) side inductance and resistance of the filter, receptively, C_c (R_c) is the capacitance (resistance) of the filter capacitor, and L_g (R_g) is the grid inductance (resistance). As the grid impedance is considered unknown, the analysis that follows is done based on the voltage at the PCC \mathbf{v}_{pcc} . By applying the Kirchhoff's circuit law to the equivalent circuit, the state-space model of the system is derived as

$$\frac{di_{conv}}{dt} = \frac{1}{L_{lc}}(-(R_{lc} + R_c)i_{conv} + R_c i_g - v_c + v_{conv}) \quad (2a)$$

$$\frac{di_g}{dt} = \frac{1}{L_{lg}}(-(R_{lg} + R_c)i_g + R_c i_{conv} + v_c - v_{pcc}) \quad (2b)$$

$$\frac{dv_c}{dt} = \frac{1}{C_c}(i_{conv} - i_g). \quad (2c)$$

By considering generic grid conditions, the voltage at the PCC can be written as

$$\mathbf{v}_{pcc} = \sum_{h \in \mathcal{H}} \mathbf{v}_{pcc,h} = \sum_{h \in \mathcal{H}} \hat{V}_h \begin{bmatrix} \cos(h\omega_g t + \varphi_h) \\ \sin(h\omega_g t + \varphi_h) \end{bmatrix}, \quad (3)$$

where h denotes the harmonic order and \mathcal{H} is the set of all harmonics.² Moreover, ω_g is the angular grid frequency, \hat{V}_h and φ_h are the amplitude and phase of the h^{th} harmonic, respectively, and they can be detected with phase-lock loops (PLLs) augmented with a decoupling network and low-pass filters (LPFs) [25]. Based on (3), the dynamics of the PCC voltage are described by

$$\frac{dv_{pcc}}{dt} = \sum_{h \in \mathcal{H}} h\omega_g \mathbf{J} \mathbf{v}_{pcc,h}, \quad \text{with } \mathbf{J} = \begin{bmatrix} 0 & -1 \\ 1 & 0 \end{bmatrix}. \quad (4)$$

Based on (2) and (4), the continuous-time state-space model of the system is

$$\frac{dx(t)}{dt} = \mathbf{F}x(t) + \mathbf{G}\mathbf{u}_{abc}(t) + \boldsymbol{\varepsilon}(t) \quad (5a)$$

$$\mathbf{y}(t) = \mathbf{C}x(t), \quad (5b)$$

where $\mathbf{x} = [i_{conv}^T \ i_g^T \ v_c^T \ v_{pcc}^T]^T$ is the state vector, $\mathbf{y} = [i_{conv}^T \ i_g^T \ v_c^T]^T$ the output vector, and $\boldsymbol{\varepsilon} = [\mathbf{0}_{6 \times 1}^T (\sum_{h \in \mathcal{H}} h\omega_g \mathbf{J} \mathbf{v}_{pcc,h})^T]^T$. Moreover, the matrices in (5) are

$$\mathbf{F} = \begin{bmatrix} -\frac{R_{lc}+R_c}{L_{lc}}\mathbf{I}_2 & \frac{R_c}{L_{lc}}\mathbf{I}_2 & -\frac{1}{L_{lc}}\mathbf{I}_2 & \mathbf{0}_{2 \times 2} \\ \frac{R_c}{L_{lg}}\mathbf{I}_2 & -\frac{R_{lg}+R_c}{L_{lg}}\mathbf{I}_2 & \frac{1}{L_{lg}}\mathbf{I}_2 & -\frac{1}{L_{lg}}\mathbf{I}_2 \\ \frac{1}{C_c}\mathbf{I}_2 & -\frac{1}{C_c}\mathbf{I}_2 & \mathbf{0}_{2 \times 2} & \mathbf{0}_{2 \times 2} \\ \mathbf{0}_{2 \times 2} & \mathbf{0}_{2 \times 2} & \mathbf{0}_{2 \times 2} & \mathbf{0}_{2 \times 2} \end{bmatrix}$$

$$\mathbf{G} = \frac{V_{dc}}{2L_{lc}}[\mathbf{I}_2 \ \mathbf{0}_{2 \times 6}]^T \mathbf{K} \quad \text{and} \quad \mathbf{C} = [\mathbf{I}_6 \ \mathbf{0}_{6 \times 2}],$$

where \mathbf{I} and $\mathbf{0}$ are the identity and zero matrices, respectively, the dimensions of which are indicated by the corresponding

²Without loss of generality, in this work, the fundamental component as well as the (negative) 5th and the (positive) 7th harmonics are considered in nominal operating conditions, i.e., $\mathcal{H} = \{1, -5, 7\}$, while the positive- and negative-sequence fundamental components are considered during faulty conditions, i.e., $\mathcal{H} = \{-1, 1\}$.

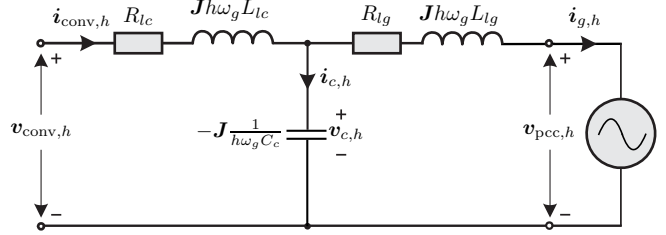


Fig. 3: Harmonic impedance model of the grid-tied converter with an *LCL* filter in the stationary ($\alpha\beta$) frame.

subscripts. Finally, using exact discretization, the discrete-time state-space model is derived as

$$\mathbf{x}(k+1) = \mathbf{A}\mathbf{x}(k) + \mathbf{B}\mathbf{u}_{abc}(k) + \mathbf{d}(k) \quad (7a)$$

$$\mathbf{y}(k) = \mathbf{C}\mathbf{x}(k), \quad (7b)$$

with

$$\mathbf{A} = e^{\mathbf{F}T_s}, \quad \mathbf{B} = \int_0^{T_s} e^{\mathbf{F}\tau} d\tau \mathbf{G}, \quad \mathbf{d} = \int_0^{T_s} e^{\mathbf{F}\tau} d\tau \boldsymbol{\varepsilon},$$

T_s being the sampling interval, and $k \in \mathbb{N}$ the discrete time step.

III. DIRECT MPC WITH FIXED SWITCHING FREQUENCY FOR ADVERSE GRID CONDITIONS

In this work, the method proposed in [26] and [24] is refined to control GTCs, with the goal to guarantee high power quality and robustness during nominal and faulty grid conditions, respectively. To this aim, the reference values of the controlled variables, i.e., the grid current, filter capacitor voltage, and converter current, are generated such that they are suitable for a wide range of operating conditions. To do so, the harmonic impedance model of the system in question is employed. In a next step, the proposed MPC scheme is designed as a multi-objective optimization problem that can address all considered cases. The formulated constrained QP underlying indirect MPC is finally solved in a computationally efficient manner in real time with an in-house solver.

A. Output References

The control objective of the proposed direct MPC is to regulate the output variables \mathbf{y} to their reference values $\mathbf{y}_{\text{ref}} = [i_{conv,\text{ref}}^T \ i_{g,\text{ref}}^T \ v_{c,\text{ref}}^T]^T$, so that the desired active P_{ref} and reactive Q_{ref} power exchange at the PCC is successfully controlled. Considering different grid conditions, the calculation of the output reference vector \mathbf{y}_{ref} can be grouped into two cases, as presented in the sequel.

1) *Nominal Operation:* The grid voltage often contains harmonics. Nevertheless, even in the presence of such persistent disturbances, the current injected into the PCC should have a low THD value in nominal operation to meet the relevant grid code. To ensure this, the grid current reference $i_{g,\text{ref}} = [i_{g,\text{ref},\alpha} \ i_{g,\text{ref},\beta}]^T$ should contain only the fundamental component, i.e.,

$$i_{g,\text{ref},\alpha} = \frac{2}{3} \frac{P_{\text{ref}} v_{pcc,\alpha,1} + Q_{\text{ref}} v_{pcc,\beta,1}}{\|\mathbf{v}_{pcc,1}\|_2^2} \quad (8a)$$

$$i_{g,\text{ref},\beta} = \frac{2}{3} \frac{P_{\text{ref}} v_{pcc,\beta,1} - Q_{\text{ref}} v_{pcc,\alpha,1}}{\|\mathbf{v}_{pcc,1}\|_2^2}. \quad (8b)$$

In a next step, the capacitor voltage reference $v_{c,\text{ref}}$ and the converter current reference $i_{\text{conv},\text{ref}}$ are calculated based on the harmonic impedance circuit, shown in Fig. 3, where the capacitor resistance R_c is neglected because of its small value. This yields

$$v_{c,\text{ref},h} = v_{\text{pcc},h} + Z_{lg,h} i_{g,\text{ref},h} \quad (9a)$$

$$i_{\text{conv},\text{ref},h} = i_{g,\text{ref},h} + Z_{c,\text{inv},h} v_{c,\text{ref},h}, \quad (9b)$$

with

$$Z_{lg,h} = R_{lg} I_2 + J h \omega_g L_{lg} \quad \text{and} \quad Z_{c,\text{inv},h} = J h \omega_g C_c.$$

Note that $i_{g,\text{ref},h} = \mathbf{0}$ for $h \neq 1$, while $i_{g,\text{ref},1} = i_{g,\text{ref}}$ is calculated from (8). Finally, the references of the capacitor voltage and the converter current are calculated by superimposing all harmonic components, i.e.,

$$v_{c,\text{ref}} = \sum_{h \in \mathcal{H}} v_{c,\text{ref},h} \quad \text{and} \quad i_{\text{conv},\text{ref}} = \sum_{h \in \mathcal{H}} i_{\text{conv},\text{ref},h}.$$

2) *Grid Faults:* During grid faults, the three-phase grid voltage—and consequently the voltage at the PCC—contains both positive- and negative-sequence voltage components at the fundamental frequency [27], i.e., $v_{\text{pcc},1}$ and $v_{\text{pcc},-1}$, respectively. Depending on the control goals, the grid current reference can be calculated based on different strategies [2]. In the following, two typical strategies are discussed.

First, the grid current is split into two components as

$$i_{g,\text{ref}} = i_{p,\text{ref}} + i_{q,\text{ref}}, \quad (10)$$

where $i_{p,\text{ref}}$ and $i_{q,\text{ref}}$ can be interpreted as the active and reactive current vectors, respectively [28]. When a balanced three-phase sinusoidal current is desired at the PCC, the balanced positive-sequence control (BPSC) strategy can be used to calculate the grid current references according to

$$i_{p,\text{ref}} = \frac{P_{\text{ref}}}{\|v_{\text{pcc},1}\|_2^2} v_{\text{pcc},1} \quad (11a)$$

$$i_{q,\text{ref}} = \frac{Q_{\text{ref}}}{\|v_{\text{pcc},1}\|_2^2} v_{\text{pcc},1}^\perp, \quad (11b)$$

where $v_{\text{pcc},1}^\perp = J v_{\text{pcc},1}$ is the (leading) orthogonal vector of $v_{\text{pcc},1}$. Note that (10) and (11) yield the same result as (8). This implies that when a balanced sinusoidal current is required at the PCC, the active and reactive powers oscillate during a grid fault because of the negative-sequence voltage component, as also shown in Section IV-B.

An alternative approach is the positive- and negative-sequence control (PNSC) strategy. This method considers both the positive- and negative-sequence fundamental voltage components in the calculation of the active and reactive current references, i.e.,

$$i_{p,\text{ref}} = \frac{P_{\text{ref}}}{\|v_{\text{pcc},1}\|_2^2 + \|v_{\text{pcc},-1}\|_2^2} (v_{\text{pcc},1} + v_{\text{pcc},-1}) \quad (12a)$$

$$i_{q,\text{ref}} = \frac{Q_{\text{ref}}}{\|v_{\text{pcc},1}\|_2^2 + \|v_{\text{pcc},-1}\|_2^2} (v_{\text{pcc},1}^\perp + v_{\text{pcc},-1}^\perp). \quad (12b)$$

By doing so, the current references consist of both positive- and negative-sequence components, resulting in a constant active power when the reactive power reference is set to

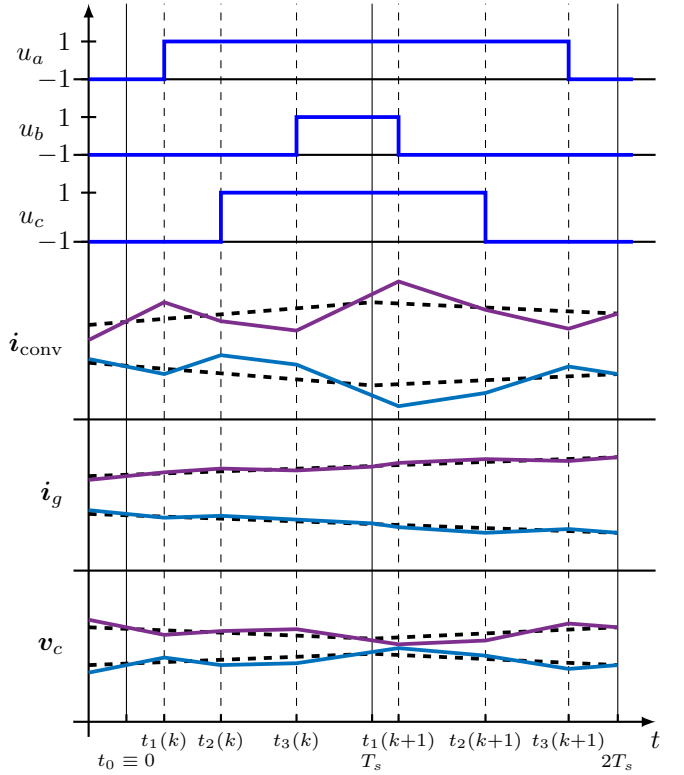


Fig. 4: Example of the evolution of the output variables (solid lines) and their references (dashed lines) in the stationary ($\alpha\beta$) frame over two sampling intervals by applying the depicted switching sequence.

zero. Finally, the capacitor voltage $v_{c,\text{ref}}$ and the converter current $i_{\text{conv},\text{ref}}$ references are calculated by following the same principle explained in Section III-A1.

B. Control Method

As a direct controller, the proposed MPC algorithm manipulates the converter switches directly. However, in contrast to typical direct control strategies, the proposed method ensures a fixed switching frequency by forcing each phase to switch once per sampling interval T_s . To this end, the vector of switching time instants t is introduced along with the corresponding switching sequence U as

$$t = [t_1 \ t_2 \ t_3]^T \quad (13)$$

$$U = [u_{abc}^T(t_0) \ u_{abc}^T(t_1) \ u_{abc}^T(t_2) \ u_{abc}^T(t_3)]^T,$$

where the switching time instants respect $0 \leq t_1 \leq t_2 \leq t_3 \leq T_s$. Moreover, $u_{abc}(t_0)$ is the switch position at the beginning of the sampling interval, i.e., $t_0 \equiv 0$, while $u_{abc}(t_i)$, with $i \in \{1, 2, 3\}$, is the switch position after one of the three phases switches at instant t_i . Considering (13) and the fact that all three phases have to switch within each T_s once, it follows that the three phases can switch in six possible chronological orders. This gives rise to six candidate switching sequences U_z with $z \in \{1, 2 \dots 6\}$, as summarized in Table I.

Having fixed the switching frequency with the above-mentioned procedure, the goal of the controller is to minimize the (approximate) rms ripple of the controlled variables. This can be achieved by designing the objective function to capture

TABLE I: Possible switching sequences for a one-step horizon.

Number of sequence	Phase with the switching transition		
	First	Second	Third
1	a	b	c
2	a	c	b
3	b	a	c
4	b	c	a
5	c	a	b
6	c	b	a

the output tracking error at the switching time instants. Moreover, to avoid arbitrary changes in the control input, its rate of change within one sampling interval is modeled and accounted for in the objective function. Therefore, the objective function is defined as

$$\begin{aligned} J = \sum_{i=1}^3 & \| \mathbf{y}_{\text{ref}}(t_i) - \mathbf{y}(t_i) \|_Q^2 + \| \boldsymbol{\Lambda}(\mathbf{y}_{\text{ref}}(T_s) - \mathbf{y}(T_s)) \|_Q^2 \\ & + \lambda_u \| \Delta \bar{\mathbf{u}}_{abc}(k) \|_2^2, \end{aligned} \quad (14)$$

where $\Delta \bar{\mathbf{u}}_{abc}(k) = \bar{\mathbf{u}}_{abc}(k) - \bar{\mathbf{u}}_{abc}(k-1)$ is the change of the averaged control input between two consecutive sampling intervals, with $\bar{\mathbf{u}}_{abc} = (\sum_{i=0}^3 \mathbf{u}_{abc}(t_i) \tilde{t}_i) / T_s$, while $\tilde{t}_i = t_{i+1} - t_i$, with $i \in \{0, 1, 2, 3\}$ and $t_4 = T_s$. Moreover, $\lambda_u > 0$ is the weighting factor that adjusts the trade-off between control and output tracking effort. Typically, λ_u should be relatively small to retain the high bandwidth of MPC. However, considering the noise-polluted measurements in a real-world setting, larger values of λ_u can prevent MPC from aggressively reacting to noise. Hence, by means of trial-and-error, the λ_u value that results in the most favorable trade-off is chosen. Additionally, the diagonal positive definite matrix $\mathbf{Q} \succ 0$ sets the priority among the tracking of the different controlled variables. In a balanced system, the grid current reference tracking is usually prioritized first to produce high-quality grid current, while the converter current error is prioritized over that the capacitor voltage as it has greater (indirect) impact on the grid current THD [24]. Nevertheless, for an imbalanced system or operation under adverse conditions, as in this work, good tracking of all output references can be equally important, implying $\mathbf{Q} = \mathbf{I}$. Finally, $\boldsymbol{\Lambda} \succ 0$ is introduced to more heavily penalize the output error at the end of the sampling interval. As explained in [24], such a penalty drives the output error at the discrete time instants to zero, effectively eliminating undesired low-frequency harmonics.

In a next step, the evolution of the system output is predicted for each candidate switching sequence \mathbf{U}_z . Given that the sampling interval T_s is much smaller than the fundamental period, the evolution of the output trajectories can be considered as linear within one T_s . Therefore, the future behavior of the system can be calculated with

$$\mathbf{y}(t_{i+1}) = \mathbf{y}(t_i) + \mathbf{m}(t_i)(t_{i+1} - t_i), \quad (15)$$

where $\mathbf{m}(t_i)$ is the gradient of the output vector when the

Algorithm 1 Fixed Switching Frequency Direct MPC

-
- Given $P_{\text{ref}}(k)$, $Q_{\text{ref}}(k)$ and $\mathbf{x}(k)$
 - 1: Calculate the output reference vector \mathbf{y}_{ref} from P_{ref} and Q_{ref}
 - 2: Enumerate the possible switching sequences \mathbf{U}_z , $z \in \{1, 2, \dots, 6\}$, and calculate the corresponding output gradient
 - 3: For each \mathbf{U}_z :
 - Detect if \mathbf{U}_z is unsuited;
 - If not, solve the QP (20). This yields \mathbf{t}_z and J_z .
 - 4: Compare the J_z of each candidate \mathbf{U}_z , and find the globally optimal solution \mathbf{t}^* and \mathbf{U}^* .
 - Return $\mathbf{t}^*(k)$ and $\mathbf{U}^*(k)$.
-

switch position $\mathbf{u}_{abc}(t_i)$ is applied, i.e.,

$$\begin{aligned} \mathbf{m}(t_i) &= \frac{\mathbf{y}(k+1) - \mathbf{y}(k)}{T_s} \\ &= \frac{\mathbf{C}((\mathbf{A} - \mathbf{I})\mathbf{x}(k) + \mathbf{B}\mathbf{u}_{abc}(t_i) + \mathbf{d}(k))}{T_s}. \end{aligned} \quad (16)$$

with $i \in \{0, 1, 2, 3\}$, $t_4 = T_s$. Moreover, as previously defined, k and $k+1$ represent the current and next discrete time steps, respectively, implying that $kT_s \leq t_i \leq (k+1)T_s$. Note that the gradients computed with (16) at instants t_1 , t_2 and t_3 depend on the state at the beginning of T_s , i.e., $\mathbf{x}(t_0) \equiv \mathbf{x}(k)$, rather than on $\mathbf{x}(t_1)$, $\mathbf{x}(t_2)$, and $\mathbf{x}(t_3)$, respectively. This is due to the aforementioned assumption of constant gradients within the sampling interval [24].

Following the same principle, the output reference is assumed to evolve linearly within one sampling interval,³ i.e.,

$$\mathbf{y}_{\text{ref}}(t) = \mathbf{y}_{\text{ref}}(k) + \mathbf{m}_{\text{ref}}(k)t, \quad (17)$$

with

$$\mathbf{m}_{\text{ref}}(k) = \frac{\mathbf{y}_{\text{ref}}(k+1) - \mathbf{y}_{\text{ref}}(k)}{T_s}. \quad (18)$$

An example of the evolution of the output variables for a given switching sequence along with their references is shown in Fig. 4.

Based on the above, the objective function can be written in the following vector form

$$J = \| \mathbf{r} - \mathbf{M}\mathbf{t} \|_{\tilde{\mathbf{Q}}}^2 + \lambda_u \| \mathbf{S}\mathbf{t} - \mathbf{w} \|_2^2, \quad (19)$$

where the matrices $\mathbf{M} \in \mathbb{R}^{24 \times 3}$, $\mathbf{S} \in \mathbb{R}^{3 \times 3}$, and $\tilde{\mathbf{Q}} \in \mathbb{R}^{24 \times 24}$ as well as the vectors $\mathbf{r} \in \mathbb{R}^{24}$ and $\mathbf{w} \in \mathbb{R}^3$ are provided in the appendix.

C. Optimization Problem

Based on the above, an optimization problem is formulated as a constrained QP for each one of the six candidate switching sequences \mathbf{U}_z . Specifically, the direct MPC problem is written in the form

$$\begin{aligned} & \underset{\mathbf{t} \in \mathbb{R}^3}{\text{minimize}} \quad \frac{1}{2} \mathbf{t}^T \mathbf{H} \mathbf{t} - \mathbf{f}^T \mathbf{t} \\ & \text{subject to} \quad 0 \leq t_1 \leq t_2 \leq t_3 \leq T_s. \end{aligned} \quad (20)$$

³Note that the references of the capacitor voltage and the converter current include harmonics at the same frequencies as that of the grid voltage. However, these harmonics are of low order, thus, the evolution of the references can still be assumed linear within one T_s .

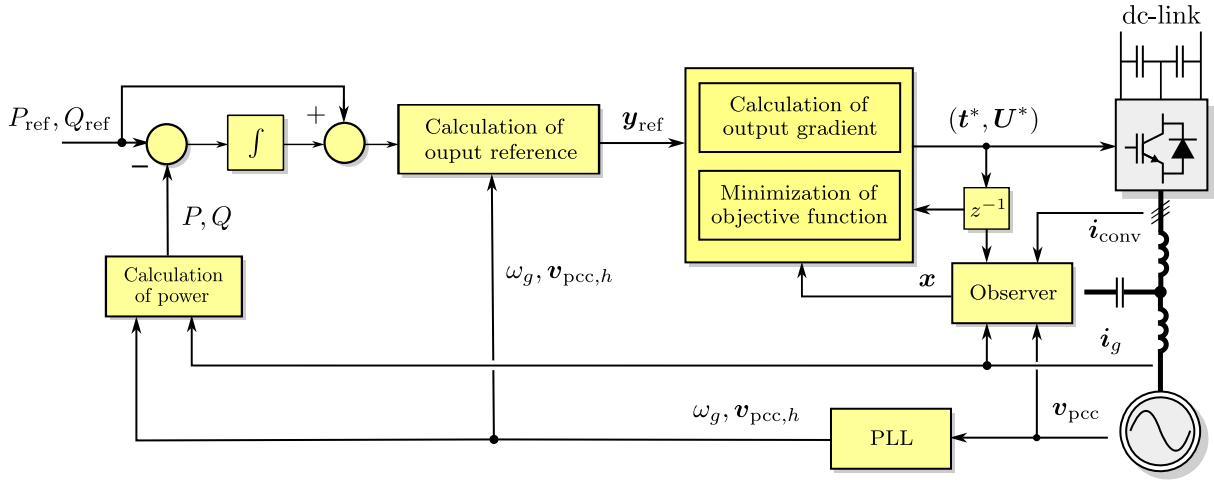


Fig. 5: Fixed switching frequency direct MPC for a three-phase grid-tied converter with an *LCL* filter.

TABLE II: Rated values of the system.

Parameter	Symbol	SI Value
Rated voltage	V_R	200 V
Rated current	I_R	9 A
Grid frequency	f_{sR}	50 Hz

TABLE III: System parameters in the SI and the p.u. system.

Parameter	SI (p.u.) symbol	SI (p.u.) value
Grid-side resistance	R_{lg} (R_{lg})	0.07Ω (0.0055)
Grid-side inductance	L_{lg} (X_{lg})	3.0 mH (0.0735)
Converter-side resistance	R_{lc} (R_{lc})	0.1Ω (0.0078)
Converter-side inductance	L_{lc} (X_{lc})	3.3 mH (0.0808)
Filter capacitor resistance	R_c (R_c)	$0.8 \text{ m}\Omega$ ($6.23 \cdot 10^{-5}$)
Filter capacitance	C_c (X_c)	$8 \mu\text{F}$ (0.0322)
Dc-link voltage	V_{dc} (V_{dc})	350 V (2.1433)

where the Hessian matrix $\mathbf{H} \in \mathbb{R}^{3 \times 3}$ and the vector $\mathbf{f} \in \mathbb{R}^3$ are

$$\mathbf{H} = \mathbf{M}^T \tilde{\mathbf{Q}} \mathbf{M} + \lambda_u \mathbf{S}^T \mathbf{S},$$

and

$$\mathbf{f} = \mathbf{M}^T \mathbf{r} + \lambda_u \mathbf{S}^T \mathbf{w}.$$

Problem (20) can be efficiently solved with the in-house solver presented in [29]. This solver is developed to fully exploit the geometry of (20) as it can quickly detect the unsuited switching sequences by a simple one-step projection. As a result, only two QPs need to be solved in the worst-case scenario, see [29] for more details.

In a last step, each QP that is eventually considered in the optimization process is solved to yield the locally optimal switching time instants t_z and the corresponding sequence U_z , along with the associated cost J_z . To find the globally optimal solution, i.e., the pair $\{t^*, U^*\}$, the costs J_z of the solved QPs are compared and the pair that corresponds to the smallest cost is selected as the to-be-applied solution [24]. The proposed direct MPC scheme is summarized in the block diagram shown in Fig. 5,⁴ while the pseudocode is provided in Algorithm 1.

⁴The capacitor voltage of the *LCL* filter is not always available in practice. To obtain the full-state information, an observer, e.g., a Kalman filter as the one designed in [29], can be used.

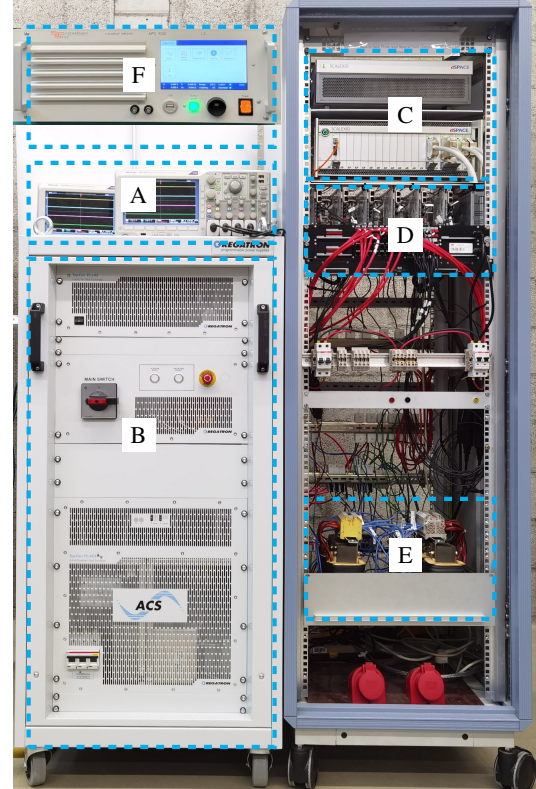


Fig. 6: Three-phase grid-tied converter with an *LCL* filter. A: Oscilloscope, B: Grid emulator, C: dSPACE SCALEXIO real-time control system, D: Power converter with Imperix PEB8038 submodules and interface, E: *LCL* filter, F: Dc source.

Finally, it is worth mentioning that MPC, being in essence a proportional controller, can be adversely affected by modeling errors and mismatches, measurement noise, etc. The influence of these is manifested as a steady-state tracking error [30]. This offset can be effectively eliminated by introducing an integrating element in the control loop. In this work, this is done by augmenting the power references with the integral of

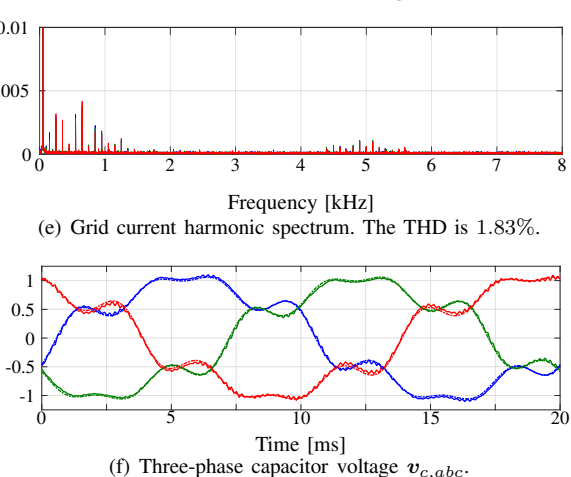
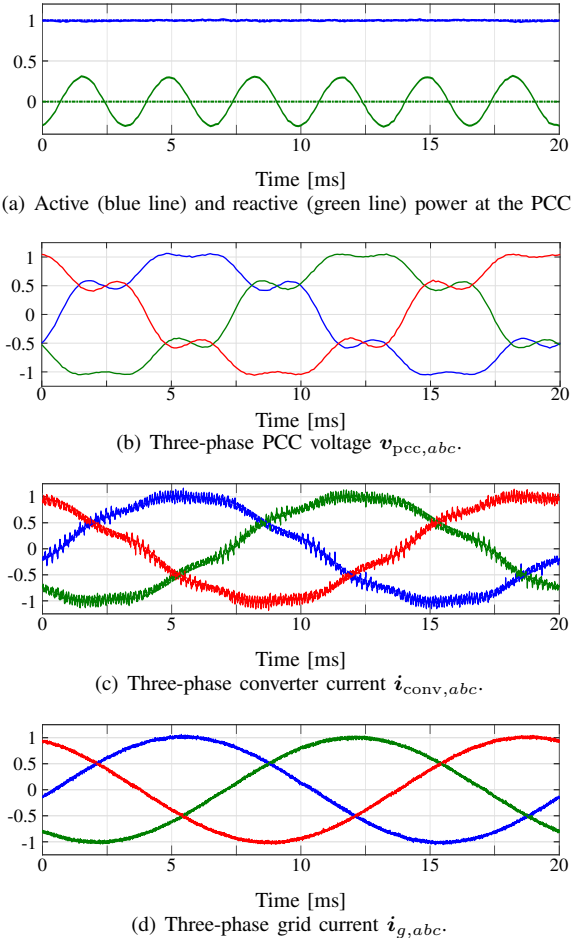


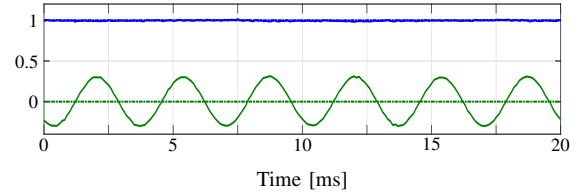
Fig. 7: Experimental results of direct MPC at steady-state operation under distorted grid conditions, $f_{sw} = 5\text{ kHz}$.

their tracking errors, see Fig. 5.⁵

IV. PERFORMANCE EVALUATION

The performance of the proposed direct MPC scheme for GTCs with LCL filters is investigated in the laboratory

⁵Note that the gain of this integral outer loop is very small, meaning that the bandwidth of the inner, MPC-based loop is significantly higher than that of the outer loop. Therefore, it can be assumed that the outer loop operates under (quasi) steady-state conditions, implying that the integrating element of the outer loop does not affect the stability of the closed-loop system.



(a) Active (blue line) and reactive (green line) power at the PCC.

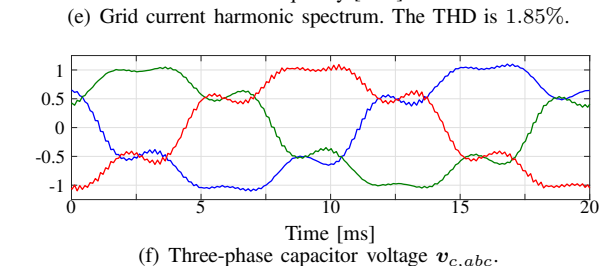
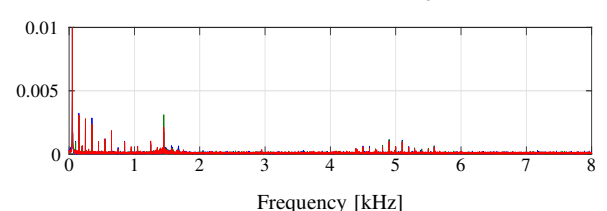
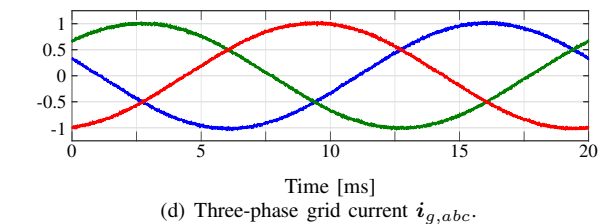
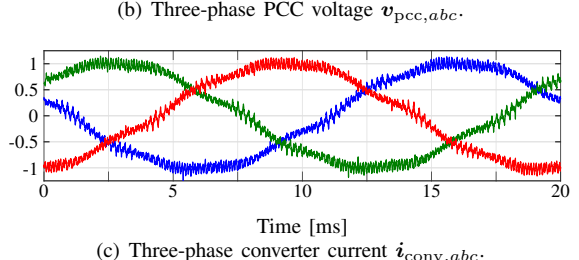
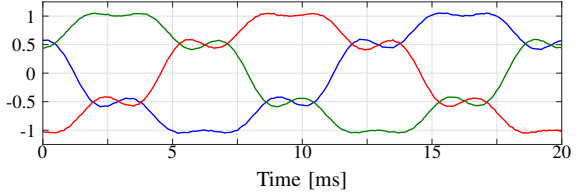
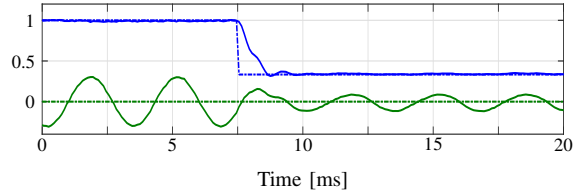
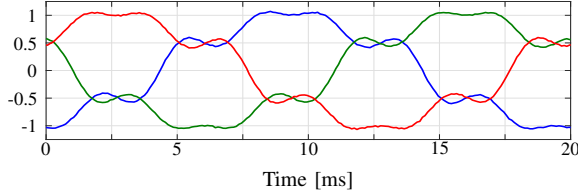


Fig. 8: Experimental results of VOC at steady-state operation under distorted grid conditions, $f_{sw} = 5\text{ kHz}$.

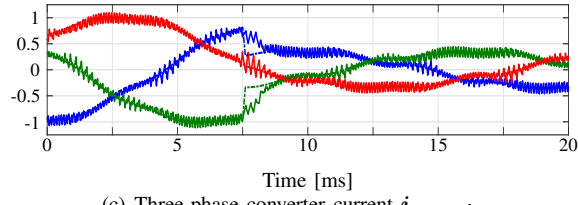
with the setup shown in Fig. 6. The converter is supplied by a stiff dc source and the grid emulator is the TC.ACS from Regatron. The real-time control platform is a dSPACE SCALEXIO system, consisting of an intel XEON processor and a Xilinx Kintex-7 field-programmable gate array (FPGA). The controller is implemented on the processor, and the data acquisition and generation of the switching signals are done on the FPGA. The rated values and the parameters of the system are given in Tables II and III, respectively. For all the



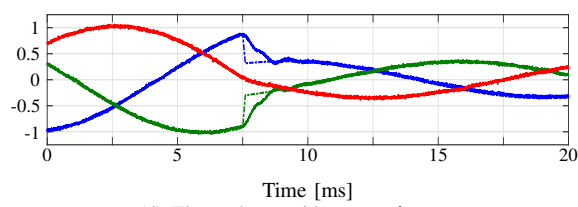
(a) Active (blue line) and reactive (green line) power at the PCC.



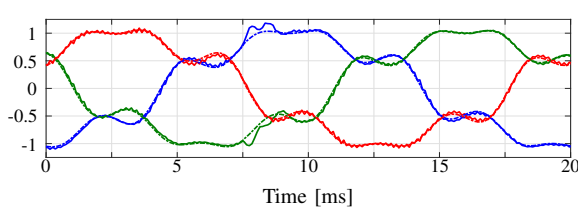
(b) Three-phase PCC voltage $v_{pcc,abc}$.



(c) Three-phase converter current $i_{conv,abc}$.



(d) Three-phase grid current $i_{g,abc}$.



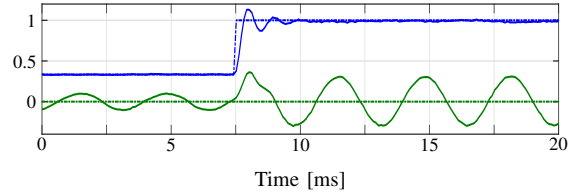
(e) Three-phase capacitor voltage $v_{c,abc}$.

Fig. 9: Experimental results of direct MPC during an active power reference step-down change under distorted grid conditions, $f_{sw} = 5 \text{ kHz}$.

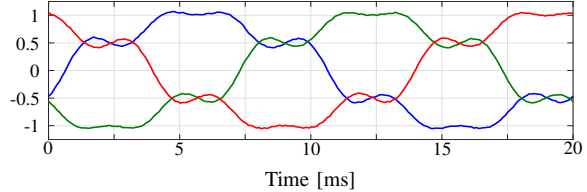
examined scenarios, the sampling frequency is chosen as $f_s = 10 \text{ kHz}$, implying a switching frequency $f_{sw} = 5 \text{ kHz}$. The weighting matrices are chosen as $\mathbf{Q} = \text{diag}(1, 1, 1, 1, 1, 1)$, $\mathbf{\Lambda} = \text{diag}(15, 15, 15)$ and $\lambda_u = 1 \cdot 10^{-3}$. Finally, all results are shown in the per unit (p.u.) system.

A. Operation under Distorted Grid Conditions

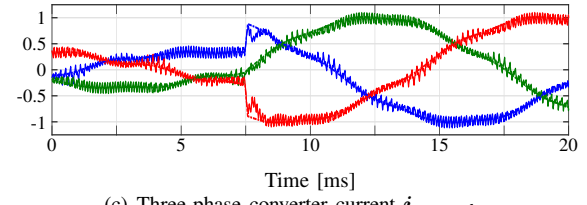
1) *Steady-State Operation:* The steady-state performance of the proposed MPC scheme is first examined for the case where the grid voltage is seriously distorted as it contains a pronounced 5th and 7th harmonic, each of which has amplitude of 0.1 p.u. For this test, the system is operating at rated power under unity power factor, i.e., $P_{\text{ref}} = 1 \text{ p.u.}$ and $Q_{\text{ref}} = 0 \text{ p.u.}$ As nominal operation is considered here, the goal is to produce a balanced three-phase grid current with as low a THD as possible. Thus, the output references are



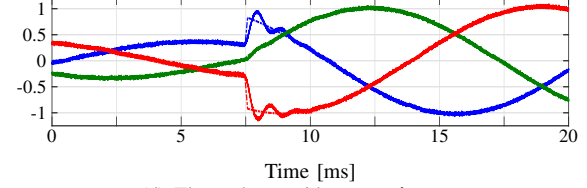
(a) Active (blue line) and reactive (green line) power at the PCC.



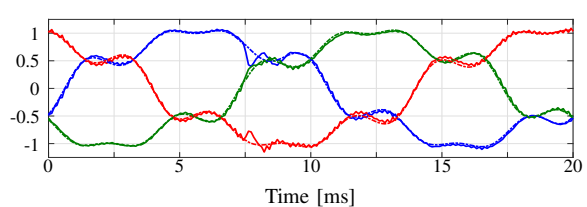
(b) Three-phase PCC voltage $v_{pcc,abc}$.



(c) Three-phase converter current $i_{conv,abc}$.



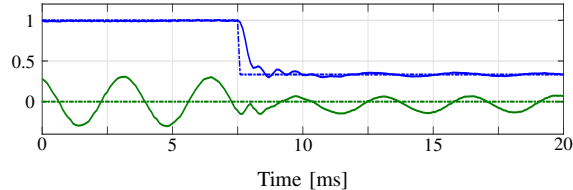
(d) Three-phase grid current $i_{g,abc}$.



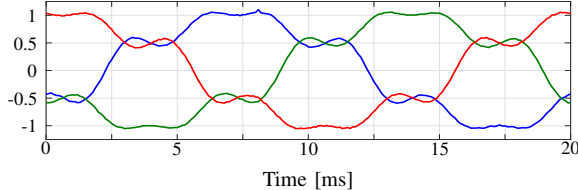
(e) Three-phase capacitor voltage $v_{c,abc}$.

Fig. 10: Experimental results of direct MPC during an active power reference step-up change under distorted grid conditions, $f_{sw} = 5 \text{ kHz}$.

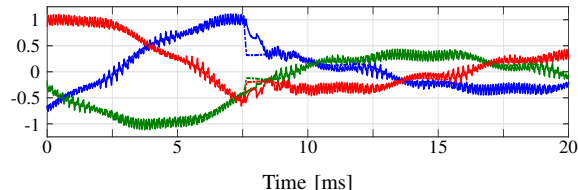
calculated with (8) and (9). Fig. 7 shows the performance of the system in consideration. As can be seen, all controlled variables, i.e., i_{conv} , i_g and v_c , track their references accurately, thus ensuring that the injected power at the PCC is of high quality. This is further demonstrated by the grid current harmonic spectrum, shown in Fig. 7(e). The high-frequency harmonics due to the switching are effectively attenuated by the *LCL* filter, while the low-frequency harmonics that result from the voltage grid harmonics are compensated for by properly regulating the filter capacitor voltage v_c and the converter current i_{conv} along their tailored reference values. As a result, the grid current THD is only 1.83%. It is noteworthy that such a low THD value is achieved despite the somewhat pronounced 11th and 13th harmonics which appear due to additional low-frequency harmonics in the grid that are not directly accounted for.



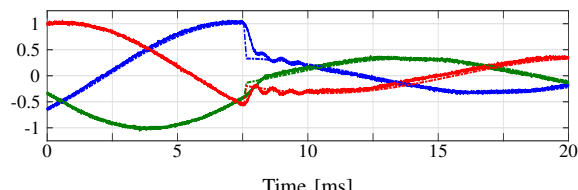
(a) Active (blue line) and reactive (green line) power at the PCC.



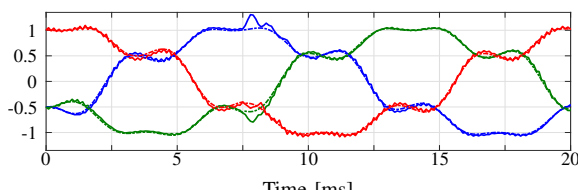
(b) Three-phase PCC voltage $v_{pcc,abc}$.



(c) Three-phase converter current $i_{conv,abc}$.



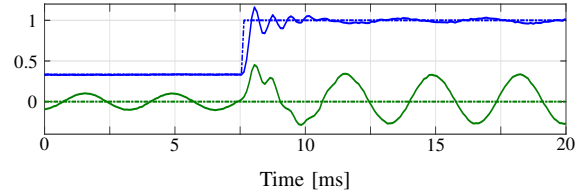
(d) Three-phase grid current $i_{g,abc}$.



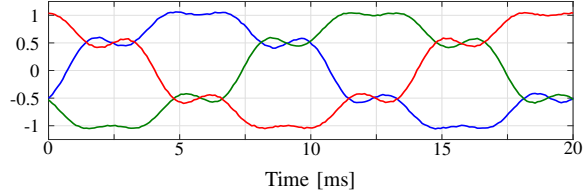
(e) Three-phase capacitor voltage $v_{c,abc}$.

Fig. 11: Experimental results of VOC during an active power reference step-down under distorted grid conditions, $f_{sw} = 5 \text{ kHz}$.

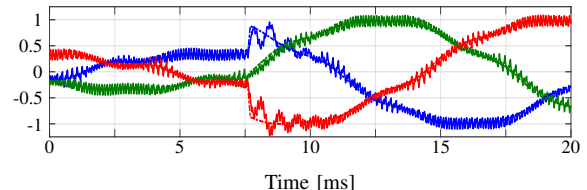
For comparison purposes, a conventional PI-based VOC strategy [5] with SVM is also implemented. This method is augmented with a capacitor-current-feedback loop for active damping [8]. Moreover, additional PI-based control loops are designed in rotating reference frames synchronized with the pronounced grid voltage harmonics to compensate for them [1]. The parameters of the PI controllers are tuned according to the optimum method [31], and the gain in the active-damping loop is tuned according to the root loci analysis [9]. As shown in Fig. 8, the steady-state performance of the conventional linear controller with a separate modulation stage is very similar to that of the proposed direct MPC in that both methods achieve similar THD values for the grid current. However, it is noticeable that the grid current spectrum produced by VOC has pronounced harmonics around the filter resonance frequency $f_{res} = 1417 \text{ Hz}$. This is in contrast to the



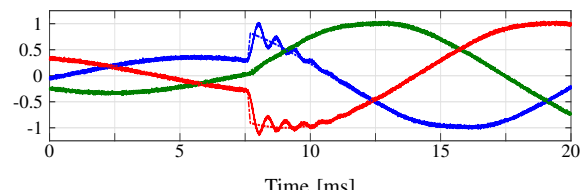
(a) Active (blue line) and reactive (green line) power at the PCC.



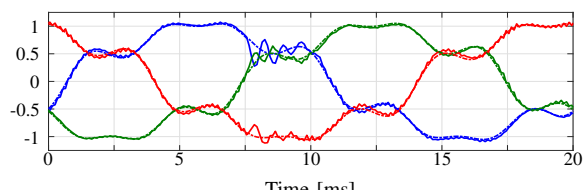
(b) Three-phase PCC voltage $v_{pcc,abc}$.



(c) Three-phase converter current $i_{conv,abc}$.



(d) Three-phase grid current $i_{g,abc}$.



(e) Three-phase capacitor voltage $v_{c,abc}$.

Fig. 12: Experimental results of VOC during an active power reference step-up change under distorted grid conditions, $f_{sw} = 5 \text{ kHz}$.

direct MPC, which demonstrates the better active damping ability of the proposed control method.

2) *Transient Operation:* While operating under a distorted grid, as described above, the dynamic behavior of the proposed direct MPC algorithm is assessed by commanding the active power reference to step down from $P_{ref} = 1 \text{ p.u.}$ to $P_{ref} = 0.33 \text{ p.u.}$ and then back up from $P_{ref} = 0.33 \text{ p.u.}$ to $P_{ref} = 1 \text{ p.u.}$ As shown in Figs. 9 and 10, the direct MPC scheme quickly regulates all the controlled variables $\mathbf{y} = [i_{conv}^T \ i_g^T \ v_c^T]^T$ —and thus the power P —to their new references with very little oscillations.

In comparison, clear oscillations can be observed in the transient performance of VOC under the same scenarios, see Figs. 11 and 12, respectively. As a result, VOC is slower than the proposed direct MPC as it takes about 2.5 ms to settle to the new operating point, while it requires more than one fundamental period to fully suppress the oscillation in the active

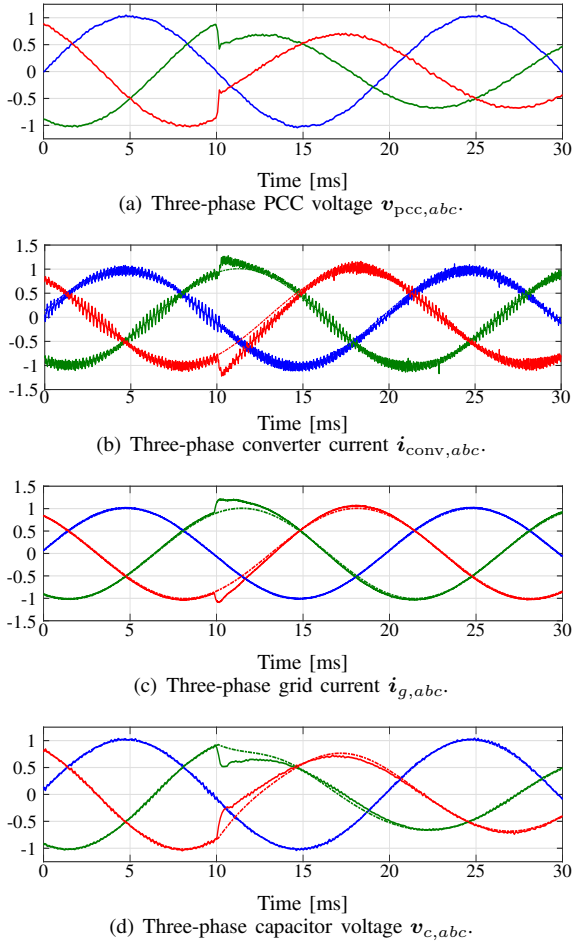


Fig. 13: Experimental results of direct MPC at a sudden grid fault, $f_{sw} = 5 \text{ kHz}$.

power. This is a typical behavior of linear controllers when applied to MIMO and high-order systems. More specifically, VOC addresses these system characteristics by decomposing the control problem into multiple single-input single-output (SISO) control loops. However, these loops tend to interact among each other in an adverse manner since they are not fully decoupled, and are thus working in an uncoordinated manner, especially during transients. In contrast to this, the direct MPC scheme accounts for all the control objectives in one constrained optimization problem and addresses them in one computational stage. Thanks to this, MPC can tellingly reject any disturbances as control and modulation act in a fully coordinated manner.

B. Grid Faults

The performance of the direct MPC scheme is also examined in the presence of grid faults. More specifically, the discussed scenario considers a phase-to-phase fault in the grid voltage. Consequently, an imbalance appears in the PCC voltage as it now contains negative-sequence components as well, i.e., the PCC voltage is of the form $v_{pcc} = v_{pcc,1} + v_{pcc,-1}$, where it is assumed that the amplitude of the positive-sequence component is $\hat{V}_1 = 0.75 \text{ p.u.}$ and that of the negative-sequence component $\hat{V}_{-1} = 0.25 \text{ p.u.}$ Moreover, the BPSC strategy is

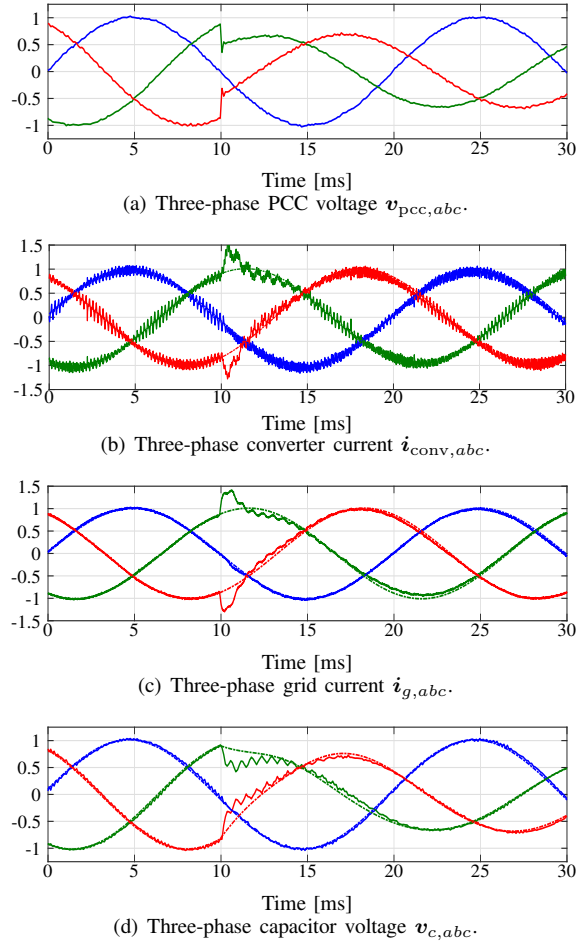
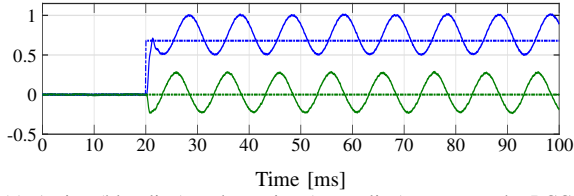


Fig. 14: Experimental results of VOC (DSRF-CC) at a sudden grid fault, $f_{sw} = 5 \text{ kHz}$.

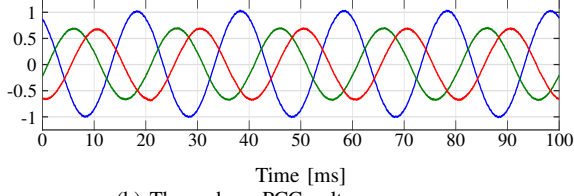
used to generate the reference values fed into the proposed direct MPC method. Fig. 13 shows the control performance when the grid suddenly experiences the described phase-to-phase fault at $t = 10 \text{ ms}$. As can be observed, the proposed direct MPC scheme responds quickly to the sudden voltage drop and the appearance of the negative-sequence voltage. Thanks to its MIMO nature and the direct control of the grid and converter currents, no overshoots appear in these variables after the fault, with their maximum value being around 1.2 p.u. As a result, all controlled variables are quickly regulated along their references, resulting in a balanced three-phase sinusoidal grid current.

For comparison purposes, a linear controller, namely, the decoupled double synchronous reference frame current controller (DSRF-CC) [12], is also implemented, while the cross-feedback decoupling network is used along with LPFs [25] to extract the positive- and negative-sequence current components. Its performance under the same scenario is shown in Fig. 14. As illustrated, the grid and converter currents exhibit overshoots, reaching values of about 1.5 p.u. after the fault. Moreover, noticeable oscillations in the controlled variables can be observed that prolong the transient phenomenon.

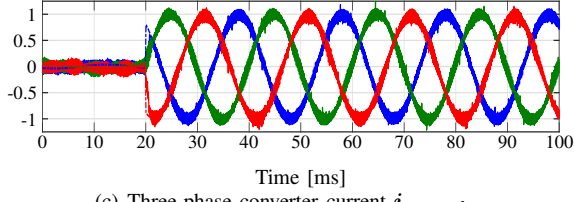
As a next scenario, the behavior of the proposed direct MPC algorithm is examined under an active power reference



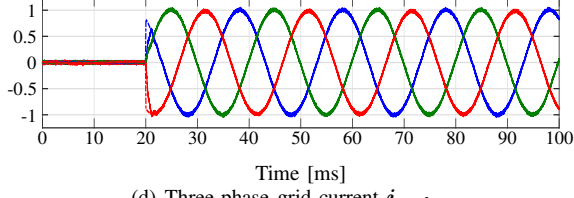
(a) Active (blue line) and reactive (green line) power at the PCC.



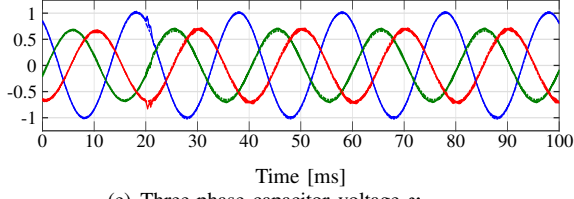
(b) Three-phase PCC voltage $v_{pcc,abc}$.



(c) Three-phase converter current $i_{conv,abc}$.



(d) Three-phase grid current $i_{g,abc}$.

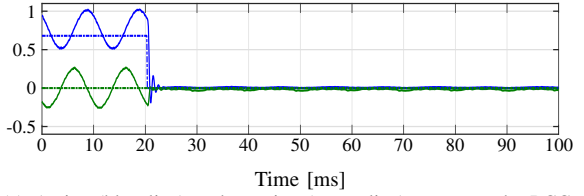


(e) Three-phase capacitor voltage $v_{c,abc}$.

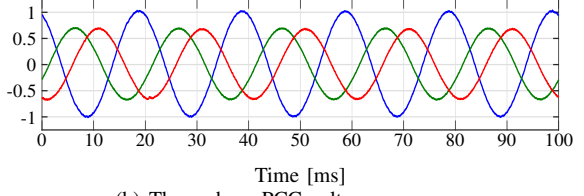
Fig. 15: Experimental results of direct MPC during an active power reference step-up change under faulty grid conditions, $f_{sw} = 5\text{ kHz}$.

step-up and step-down change. Figs. 15 and 16 show the behavior of the system for the step-up and step-down change, respectively, which is commanded at $t = 20\text{ ms}$. As shown, in both cases, the system reaches the new operating point just within 2 ms, while no oscillations are observed. Moreover, the grid currents are sinusoidal, with low harmonic content, and well balanced, as expected with the BPSC strategy. The performance of DSRF-CC under the same scenario is shown in Figs. 17 and 18. As can be seen, its transient performance is much slower compared to that of direct MPC. Especially during the power reference step-down change, not only large oscillations appear at the beginning of the transient, but also it takes almost 80 ms—which is about 40 times greater than the time required by the direct MPC scheme—to finally settle to the new operating point.

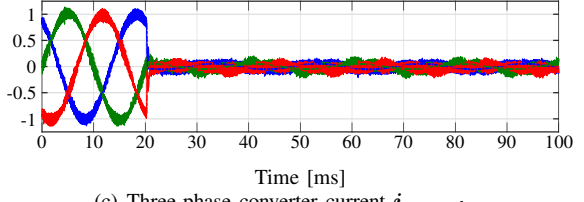
Another interesting transient scenario is the transition be-



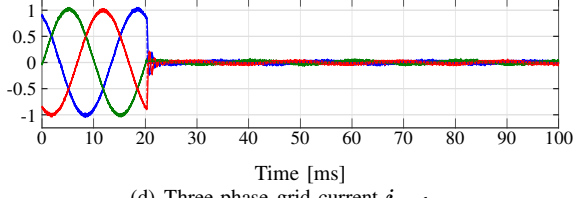
(a) Active (blue line) and reactive (green line) power at the PCC.



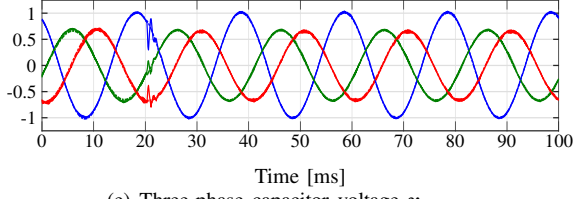
(b) Three-phase PCC voltage $v_{pcc,abc}$.



(c) Three-phase converter current $i_{conv,abc}$.



(d) Three-phase grid current $i_{g,abc}$.

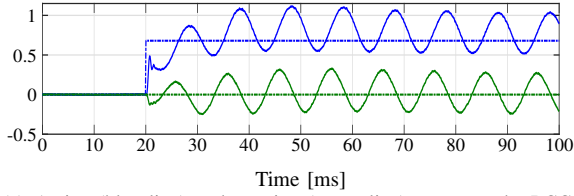


(e) Three-phase capacitor voltage $v_{c,abc}$.

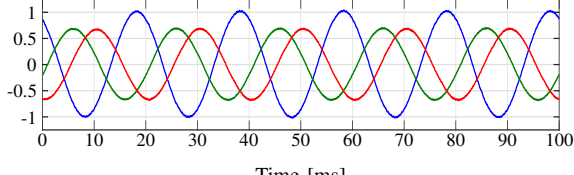
Fig. 16: Experimental results of direct MPC during an active power reference step-down change under faulty grid conditions, $f_{sw} = 5\text{ kHz}$.

tween the two methods that provide the output references, see Section III-A2. As shown in Figs. 19 and 20, direct MPC can seamlessly switch between BPSC and PNSC strategies, producing either a balanced three-phase current or a constant active power, respectively. In comparison, the transitions of DSRF-CC between the two methods require significantly more time, see Figs. 21 and 22. Similar to the dynamic performance shown in Figs. 17 and 18, DSRF-CC needs about 80 ms to finally reach the new reference values provided by either BPSC or PNSC. This slow dynamic response is mainly due to the LPFs in the current control loops,⁶ which are necessary in the DSRF-CC scheme for attenuating the oscillations caused by the interaction between the positive- and negative-sequence

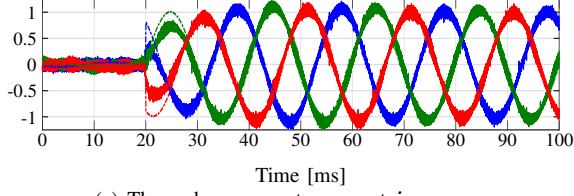
⁶The cut-off frequency was set to $\omega_f = \omega_g/\sqrt{2}$, as suggested by many previous studies, e.g., [2], [25]. Note that the control tends to be unstable when the cut-off frequency is tuned to be either too high or too low, see [2, Section 10.3].



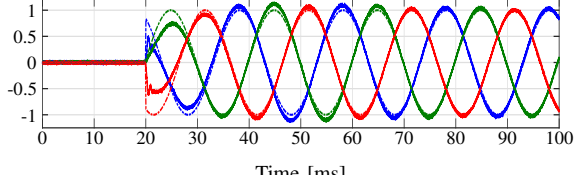
(a) Active (blue line) and reactive (green line) power at the PCC.



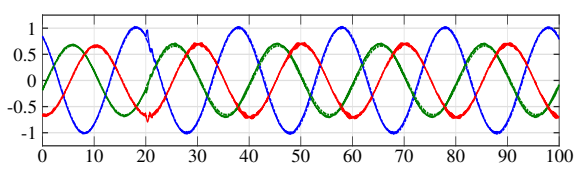
(b) Three-phase PCC voltage $v_{pcc,abc}$.



(c) Three-phase converter current $i_{conv,abc}$.



(d) Three-phase grid current $i_{g,abc}$.



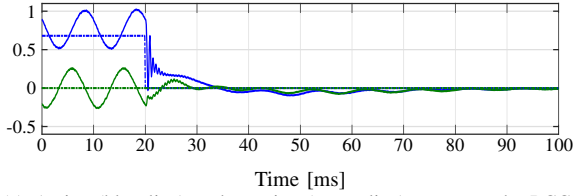
(e) Three-phase capacitor voltage $v_{c,abc}$.

Fig. 17: Experimental results of VOC (DSRF-CC) during an active power reference step-up change under faulty grid conditions, $f_{sw} = 5\text{ kHz}$.

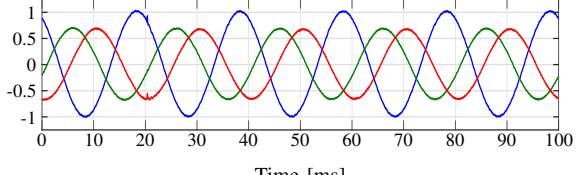
current vectors.

V. CONCLUSION

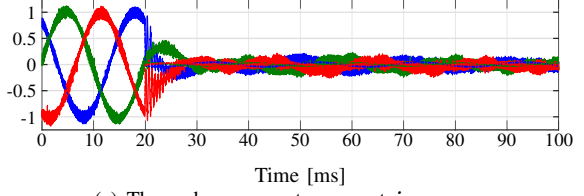
This article presented a direct MPC strategy for grid-tied converters (GTCs) with LCL filters that can successfully operate the system under both nominal and faulty grid conditions. To achieve this, the reference values of the controlled variables, i.e., the grid and converter current as well as the filter capacitor voltage, are generated to account for the different grid conditions. Subsequently, a versatile system modeling that relies on the gradient of the system output is employed to tackle the MIMO characteristics of the system in question. In doing so, the design of the control and modulation problems as a unified problem is enabled. As a result, the proposed single control structure is suitable for all different scenarios without requiring adjustments and/or retuning when the operating



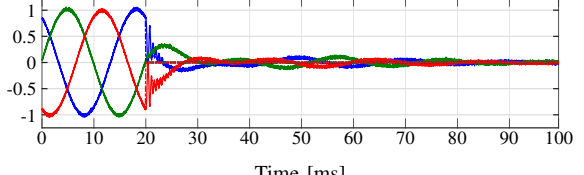
(a) Active (blue line) and reactive (green line) power at the PCC.



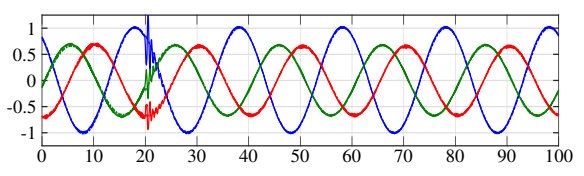
(b) Three-phase PCC voltage $v_{pcc,abc}$.



(c) Three-phase converter current $i_{conv,abc}$.



(d) Three-phase grid current $i_{g,abc}$.

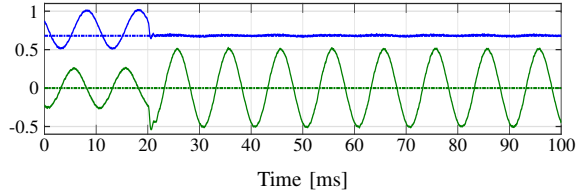


(e) Three-phase capacitor voltage $v_{c,abc}$.

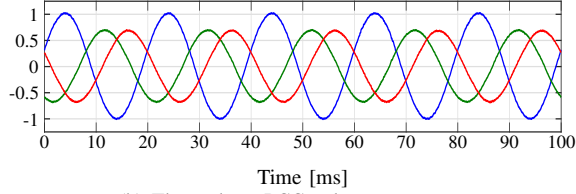
Fig. 18: Experimental results of VOC (DSRF-CC) during an active power reference step-down change under faulty grid conditions, $f_{sw} = 5\text{ kHz}$.

conditions change. This is in stark contrast to conventional control methods that rely on linear control techniques as these decompose the MIMO control problem into several SISO control loops that interact with each other in an adverse manner. For this reason, retuning and gain scheduling are required when the operating point changes, leading to a cumbersome tuning procedure and a low bandwidth. These problems are further aggravated since linear control techniques—as opposed to the proposed direct MPC method—are augmented with an active damping loop, which tends to further compromise the performance and design procedure. The superior performance of the proposed direct MPC method was verified with the presented experimental studies that related to operation under nominal conditions characterized by persistent disturbances as well as faulty grid conditions.

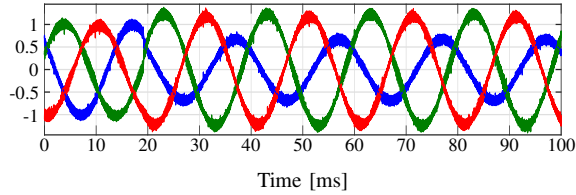
The main challenge in implementing the proposed direct



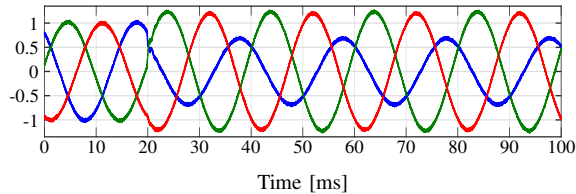
(a) Active (blue line) and reactive (green line) power at the PCC.



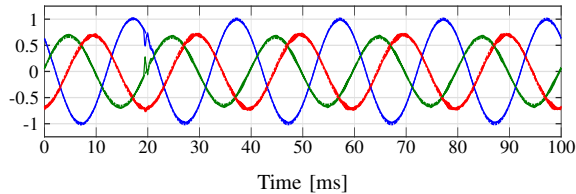
(b) Three-phase PCC voltage $v_{pcc,abc}$.



(c) Three-phase converter current $i_{conv,abc}$.



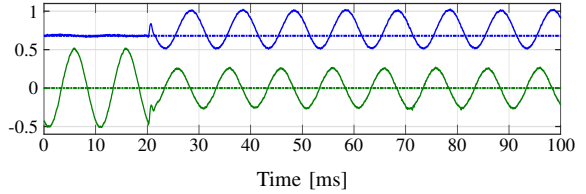
(d) Three-phase grid current $i_{g,abc}$.



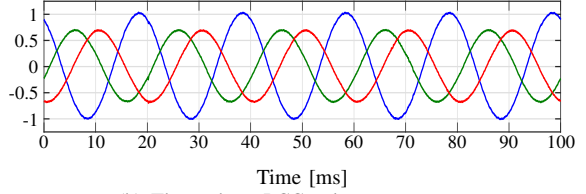
(e) Three-phase capacitor voltage $v_{c,abc}$.

Fig. 19: Experimental results of direct MPC during a change from BPSC to PNSC under faulty grid conditions, $f_{sw} = 5\text{ kHz}$.

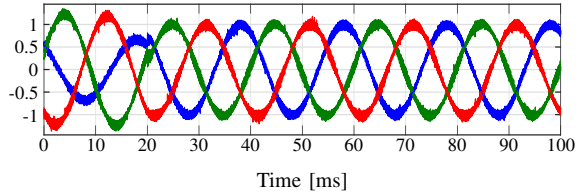
MPC strategy is its high computational burden. Although an efficient in-house solver was adopted, high-performance control hardware is still required to solve the underlying optimization problem in real time. Methods for further reducing the computational complexity can be investigated in future work. Moreover, although some guidelines about the tuning of the weighting factors of the MPC objective function are provided in this work, tuning can still be laborious as it is tailored to the problem at hand and case-dependent. Additionally, this work demonstrated the advantages of the direct MPC strategy in terms of controller bandwidth and robustness against grid faults. Its potential can be further explored by considering other more challenging scenarios encountered in modern grids. For example, the current limiting ability of the controller at voltage sags and phase jumps as well as its performance for grid support, are possible research directions.



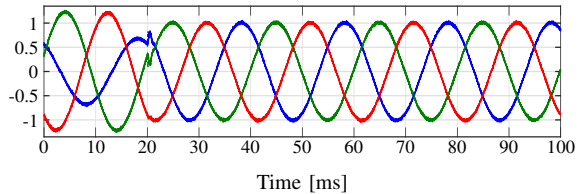
(a) Active (blue line) and reactive (green line) power at the PCC.



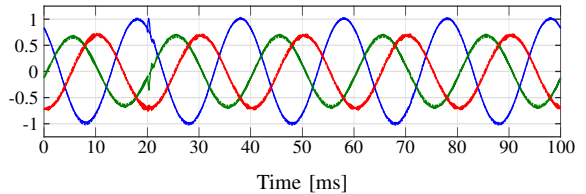
(b) Three-phase PCC voltage $v_{pcc,abc}$.



(c) Three-phase converter current $i_{conv,abc}$.



(d) Three-phase grid current $i_{g,abc}$.



(e) Three-phase capacitor voltage $v_{c,abc}$.

Fig. 20: Experimental results of direct MPC during a change from PNSC to BPSC under faulty grid conditions, $f_{sw} = 5\text{ kHz}$.

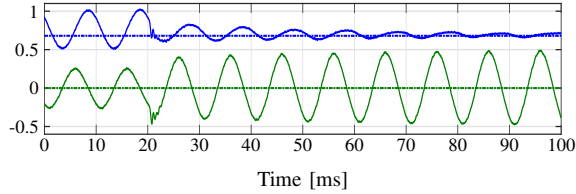
APPENDIX

The vector $\mathbf{r} \in \mathbb{R}^{24}$ and matrix $\mathbf{M} \in \mathbb{R}^{24 \times 3}$ in (19) are

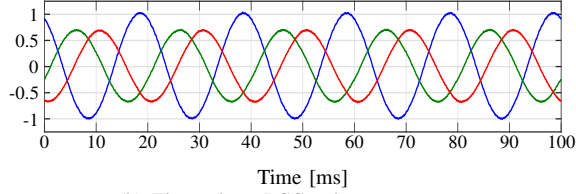
$$\mathbf{r} = \begin{bmatrix} \mathbf{y}_{ref}(t_0) - \mathbf{y}(t_0) \\ \mathbf{y}_{ref}(t_0) - \mathbf{y}(t_0) \\ \mathbf{y}_{ref}(t_0) - \mathbf{y}(t_0) \\ \Lambda(\mathbf{y}_{ref}(T_s) - \mathbf{y}(t_0) - \mathbf{m}(t_3)T_s) \end{bmatrix}$$

and

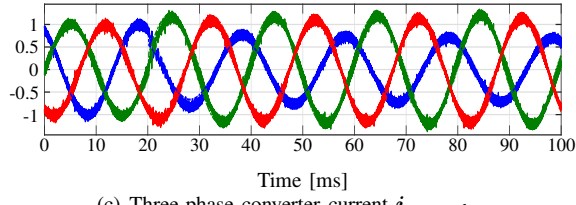
$$\mathbf{M} = \begin{bmatrix} \mathbf{m}_{t_0} & \mathbf{0}_6 & \mathbf{0}_6 \\ \mathbf{m}_0 & \mathbf{m}_{t_1} & \mathbf{0}_6 \\ \mathbf{m}_0 & \mathbf{m}_1 & \mathbf{m}_{t_2} \\ \Lambda\mathbf{m}_0 & \Lambda\mathbf{m}_1 & \Lambda\mathbf{m}_2 \end{bmatrix}$$



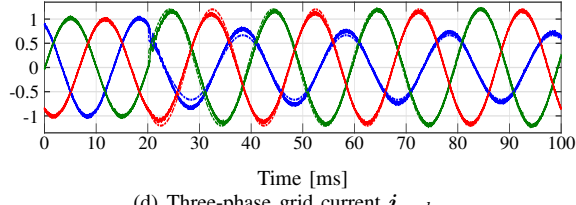
(a) Active (blue line) and reactive (green line) power at the PCC.



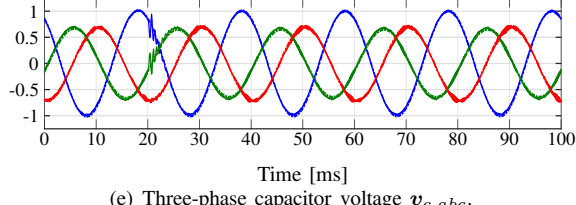
(b) Three-phase PCC voltage $v_{pcc,abc}$.



(c) Three-phase converter current $i_{conv,abc}$.



(d) Three-phase grid current $i_{g,abc}$.



(e) Three-phase capacitor voltage $v_{c,abc}$.

Fig. 21: Experimental results of VOC (DSRF-CC) during a change from BPSC to PNSC under faulty grid conditions, $f_{sw} = 5$ kHz.

with

$$\begin{aligned}\mathbf{m}_{t_i} &= \mathbf{m}(t_i) - \mathbf{m}_{\text{ref}} \\ \mathbf{m}_i &= \mathbf{m}(t_i) - \mathbf{m}(t_{i+1}),\end{aligned}$$

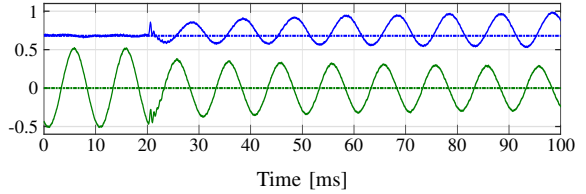
where $i \in \{0, 1, 2\}$. Moreover, the matrix $\mathbf{S} \in \mathbb{R}^{3 \times 3}$ and the vector $\mathbf{w} \in \mathbb{R}^3$ are

$$\begin{aligned}\mathbf{S} &= \frac{1}{T_s} \begin{bmatrix} \Delta \mathbf{u}_{abc}(t_1) & \Delta \mathbf{u}_{abc}(t_2) & \Delta \mathbf{u}_{abc}(t_3) \end{bmatrix}, \\ \mathbf{w} &= \mathbf{u}_{abc}(t_3) - \bar{\mathbf{u}}_{abc}(k-1),\end{aligned}$$

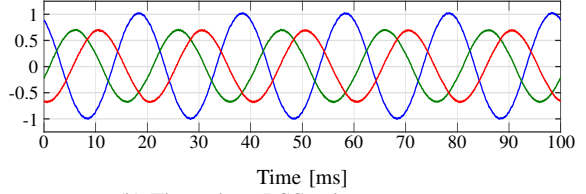
with

$$\Delta \mathbf{u}(t_i) = \mathbf{u}_{abc}(t_i) - \mathbf{u}_{abc}(t_{i-1}), \quad i \in \{1, 2, 3\}.$$

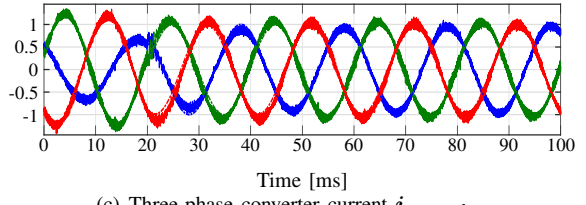
Finally, $\tilde{\mathbf{Q}} = \text{diag}(\mathbf{Q}, \mathbf{Q}, \mathbf{Q}, \mathbf{Q})$.



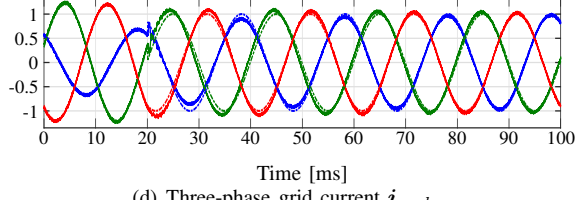
(a) Active (blue line) and reactive (green line) power at the PCC.



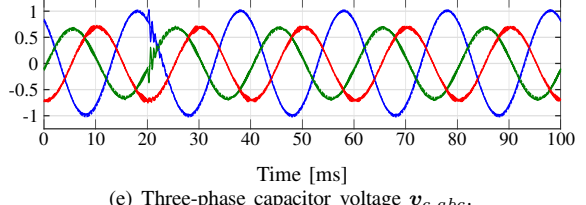
(b) Three-phase PCC voltage $v_{pcc,abc}$.



(c) Three-phase converter current $i_{conv,abc}$.



(d) Three-phase grid current $i_{g,abc}$.



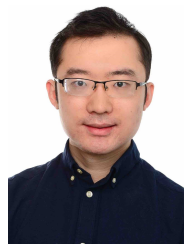
(e) Three-phase capacitor voltage $v_{c,abc}$.

Fig. 22: Experimental results of VOC (DSRF-CC) during a change from PNSC to BPSC under faulty grid conditions, $f_{sw} = 5$ kHz.

REFERENCES

- [1] F. Blaabjerg, R. Teodorescu, M. Liserre, and A. Timbus, "Overview of control and grid synchronization for distributed power generation systems," *IEEE Trans. Ind. Electron.*, vol. 53, no. 5, pp. 1398–1409, Oct. 2006.
- [2] R. Teodorescu, M. Liserre, and P. Rodriguez, *Grid converters for photovoltaic and wind power systems*. John Wiley & Sons, 2011.
- [3] IEEE Std 519-2014 (Revision of IEEE Std 519-1992), "IEEE recommended practices and requirements for harmonic control in electrical power systems," pp. 1–29, Jun. 2014.
- [4] IEC 61000-2-4, "Electromagnetic compatibility (EMC)-part 2-4: Environment-compatibility levels in industrial plants for low-frequency conducted disturbances," Sep. 2002.
- [5] M. Liserre, F. Blaabjerg, and S. Hansen, "Design and control of an LCL-filter-based three-phase active rectifier," *IEEE Trans. Ind. Appl.*, vol. 41, no. 5, pp. 1281–1291, Sep./Oct. 2005.
- [6] M. Liserre, R. Teodorescu, and F. Blaabjerg, "Stability of photovoltaic and wind turbine grid-connected inverters for a large set of grid impedance values," *IEEE Trans. Power Electron.*, vol. 21, no. 1, pp. 263–272, Jan. 2006.

- [7] J. Dannehl, F. W. Fuchs, S. Hansen, and P. B. Thøgersen, "Investigation of active damping approaches for PI-based current control of grid-connected pulse width modulation converters with *LCL* filters," *IEEE Trans. Ind. Appl.*, vol. 46, no. 4, pp. 1509–1517, Jul./Aug. 2010.
- [8] C. Bao, X. Ruan, X. Wang, W. Li, D. Pan, and K. Weng, "Step-by-step controller design for *LCL*-type grid-connected inverter with capacitor-current-feedback active-damping," *IEEE Trans. Power Electron.*, vol. 29, no. 3, pp. 1239–1253, Mar. 2014.
- [9] S. G. Parker, B. P. McGrath, and D. G. Holmes, "Regions of active damping control for *LCL* filters," *IEEE Trans. Ind. Appl.*, vol. 50, no. 1, pp. 424–432, Jan./Feb. 2014.
- [10] R. Peña-Alzola, M. Liserre, F. Blaabjerg, M. Ordóñez, and Y. Yang, "*LCL*-filter design for robust active damping in grid-connected converters," *IEEE Trans. Ind. Informat.*, vol. 10, no. 4, pp. 2192–2203, Nov. 2014.
- [11] M. H. Bollen and L. Zhang, "Different methods for classification of three-phase unbalanced voltage dips due to faults," *Electr. Power Syst. Res.*, vol. 66, no. 1, pp. 59–69, 2003.
- [12] H.-S. Song and K. Nam, "Dual current control scheme for PWM converter under unbalanced input voltage conditions," *IEEE Trans. Ind. Electron.*, vol. 46, no. 5, pp. 953–959, Oct. 1999.
- [13] P. Karamanakos, E. Liegmann, T. Geyer, and R. Kennel, "Model predictive control of power electronic systems: Methods, results, and challenges," *IEEE Open J. Ind. Appl.*, vol. 1, pp. 95–114, 2020.
- [14] P. Karamanakos and T. Geyer, "Guidelines for the design of finite control set model predictive controllers," *IEEE Trans. Power Electron.*, vol. 35, no. 7, pp. 7434–7450, Jul. 2020.
- [15] T. Geyer, "A comparison of control and modulation schemes for medium-voltage drives: Emerging predictive control concepts versus PWM-based schemes," *IEEE Trans. Ind. Appl.*, vol. 47, no. 3, pp. 1380–1389, May/Jun. 2011.
- [16] J. Scoltock, T. Geyer, and U. K. Madawala, "A model predictive direct current control strategy with predictive references for MV grid-connected converters with *LCL*-filters," *IEEE Trans. Power Electron.*, vol. 30, no. 10, pp. 5926–5937, Oct. 2015.
- [17] P. Falkowski and A. Sikorski, "Finite control set model predictive control for grid-connected ac–dc converters with *LCL* filter," *IEEE Trans. Ind. Electron.*, vol. 65, no. 4, pp. 2844–2852, Apr. 2018.
- [18] D. G. Holmes and T. A. Lipo, *Pulse Width Modulation for Power Converters: Principles and Practice*. Piscataway, NJ: IEEE Press, 2003.
- [19] C. Xue, D. Zhou, and Y. Li, "Hybrid model predictive current and voltage control for *LCL*-filtered grid-connected inverter," *IEEE J. Emerg. Sel. Topics Power Electron.*, vol. 9, no. 5, pp. 5747–5760, Oct. 2021.
- [20] M. Rossi, P. Karamanakos, and F. Castelli-Dezza, "An indirect model predictive control method for grid-connected three-level neutral point clamped converters with *LCL* filters," *IEEE Trans. Ind. Appl.*, vol. 58, no. 3, pp. 3750–3768, May/Jun. 2022.
- [21] F. Toso, A. Favato, R. Torchio, P. Alotto, and S. Bolognani, "Continuous control set model predictive current control of a microgrid-connected PWM inverter," *IEEE Trans. Power Syst.*, vol. 36, no. 1, pp. 415–425, Jan. 2021.
- [22] S. Vazquez, A. Marquez, R. Aguilera, D. Quevedo, J. I. Leon, and L. G. Franquelo, "Predictive optimal switching sequence direct power control for grid-connected power converters," *IEEE Trans. Ind. Electron.*, vol. 62, no. 4, pp. 2010–2020, Apr. 2015.
- [23] A. Mora, R. Cárdenas-Dobson, R. P. Aguilera, A. Angulo, F. Donoso, and J. Rodríguez, "Computationally efficient cascaded optimal switching sequence MPC for grid-connected three-level NPC converters," *IEEE Trans. Power Electron.*, vol. 34, no. 12, pp. 12 464–12 475, Dec. 2019.
- [24] P. Karamanakos, M. Nahalparvari, and T. Geyer, "Fixed switching frequency direct model predictive control with continuous and discontinuous modulation for grid-tied converters with *LCL* filters," *IEEE Trans. Control Syst. Technol.*, vol. 29, no. 4, pp. 1503–1518, Jul. 2021.
- [25] P. Rodriguez, J. Pou, J. Bergas, J. I. Candela, R. P. Burgos, and D. Boroyevich, "Decoupled double synchronous reference frame PLL for power converters control," *IEEE Trans. Power Electron.*, vol. 22, no. 2, pp. 584–592, Mar. 2007.
- [26] P. Karamanakos, R. Mattila, and T. Geyer, "Fixed switching frequency direct model predictive control based on output current gradients," in *Proc. IEEE Ind. Electron. Conf.*, Washington, D.C., USA, Oct. 2018, pp. 2329–2334.
- [27] M. H. Bollen and L. Zhang, "Different methods for classification of three-phase unbalanced voltage dips due to faults," *Electr. Power Syst. Res.*, vol. 66, no. 1, pp. 59–69, 2003.
- [28] H. Akagi, E. H. Watanabe, and M. Arede, *Instantaneous power theory and applications to power conditioning*. John Wiley & Sons, 2017.
- [29] Q. Yang, P. Karamanakos, W. Tian, X. Gao, X. Li, T. Geyer, and R. Kennel, "Computationally efficient fixed switching frequency direct model predictive control," *IEEE Trans. Power Electron.*, vol. 37, no. 3, pp. 2761–2777, Mar. 2022.
- [30] G. Pannocchia, M. Gabiccini, and A. Artoni, "Offset-free MPC explained: Novelties, subtleties, and applications," *IFAC-PapersOnLine*, vol. 48, no. 23, pp. 342–351, 2015.
- [31] V. Blasko and V. Kaura, "A novel control to actively damp resonance in input *LC* filter of a three-phase voltage source converter," *IEEE Trans. Ind. Appl.*, vol. 33, no. 2, pp. 542–550, Mar./Apr. 1997.



Qifan Yang received the B.Eng. degree in electrical engineering Xi'an Jiaotong University, Xi'an, Shaanxi, China, in 2016, and the M.Sc. degree in electrical power engineering from Technical University of Munich, Munich, Germany, in 2019. Since 2019, he has been pursuing the Ph.D. degree at the Chair of Electrical Drive Systems and Power Electronics, Technical University of Munich (TUM), Germany. His research interests include optimal control, power electronics and electrical drives.



Petros Karamanakos (M'14 – SM'19) received the Diploma and Ph.D. degrees in electrical and computer engineering from the National Technical University of Athens (NTUA), Athens, Greece, in 2007, and 2013, respectively.

From 2010 to 2011 he was with the ABB Corporate Research Center, Baden-Dättwil, Switzerland, where he worked on model predictive control strategies for medium-voltage drives. From 2013 to 2016 he was a PostDoc Research Associate in the Chair of Electrical Drive Systems and Power Electronics, Technische Universität München, Munich, Germany. Since 2016, he has been with the Faculty of Information Technology and Communication Sciences, Tampere University, Tampere, Finland, where he is currently an Associate Professor. His main research interests lie at the intersection of optimal control, mathematical programming and power electronics, including model predictive control and optimal modulation for utility-scale power converters and ac variable speed drives.

Dr. Karamanakos received the 2014 Third Best Paper Award of the IEEE Transactions on Industry Applications and four Prize Paper Awards at conferences. He serves as an Associate Editor of the IEEE Transactions on Power Electronics, IEEE Journal of Emerging and Selected Topics in Power Electronics, and IEEE Transactions on Industry Applications. He has been a Regional Distinguished Lecturer of the IEEE Power Electronics Society since 2022.



Wei Tian (S'16 - M'22) received the B.Eng. degree in electrical engineering and automation from Central South University (CSU), Changsha, China, in 2012 and the M.Sc. degree in electrical power engineering from RWTH Aachen University, Aachen, Germany, in 2015. Since 2016, he has been pursuing the Ph.D. degree at the Chair of Electrical Drive Systems and Power Electronics, and the Chair of High-Power Converter Systems, Technical University of Munich (TUM), Munich, Germany. His research interests include power electronics and electrical drives, model predictive control, and modular multilevel converter.



Tobias Geyer (M'08 – SM'10 – F'22) received the Dipl.-Ing. degree in electrical engineering, the Ph.D. in control engineering, and the Habilitation degree in power electronics from ETH Zurich in the years 2000, 2005, and 2017, respectively.

After his Ph.D., he spent three years at GE Global Research, Munich, Germany, three years at the University of Auckland, Auckland, New Zealand, and eight years at ABB's Corporate Research Centre, Baden-Dättwil, Switzerland. In 2020, he joined ABB's Medium-Voltage Drive division as R&D platform manager of the ACS6080. In 2022, he became a Corporate Executive Engineer. He has been an extraordinary Professor at Stellenbosch University, Stellenbosch, South Africa, since 2017.

He is the author of more than 40 patent families, 160 publications and the book "Model predictive control of high-power converters and industrial drives" (Wiley, 2016). He teaches a regular course on model predictive control at ETH Zurich. His research interests include medium-voltage and low-voltage drives, utility-scale power converters, optimized pulse patterns and model predictive control.

Dr. Geyer received the IEEE PELS Modeling and Control Technical Achievement Award in 2022, the Semikron Innovation Award in 2021, and the Nagamori Award in 2021. He also received two Prize Paper Awards of IEEE transactions and three Prize Paper Awards at IEEE conferences. He is a former Associate Editor of the IEEE Transactions on Industry Applications (from 2011 until 2014) and the IEEE Transactions on Power Electronics (from 2013 until 2019). He was an International Program Committee Vice Chair of the IFAC conference on Nonlinear Model Predictive Control in Madison, WI, USA, in 2018. Dr. Geyer is a Distinguished Lecturer of the IEEE Power Electronics Society from the year 2020 until 2023.



Marcelo Lobo Heldwein (S'99-M'08-SM'13) received the bachelor and master degrees in electrical engineering from the Federal University of Santa Catarina (UFSC), Brazil, in 1997 and 1999, respectively, and his doctoral degree from the Swiss Federal Institute of Technology (ETH Zurich), Switzerland, in 2007.

He is a Professor at the Technical University of Munich, Germany, leading the research group at the Chair of High-Power Converter Systems.

From 1999 to 2003, he worked with industry, including R&D activities at the Power Electronics Institute in Brazil and Emerson Network Power in Brazil and Sweden. He was a Postdoctoral Fellow at the ETH Zurich and the UFSC from 2007 to 2009. He was an Associate Professor with the Department of Electronics and Electrical Engineering at the UFSC from 2010 to 2022. Dr. Heldwein is a senior member of the IEEE, a member of the Brazilian Power Electronic Society (SOBRAEP), and a member of the Advisory Board of PCIM Europe.

His research focuses on power converters and motor drives, including their topologies, modeling, design, and control. The research is motivated to develop sustainable and intelligent solutions to the challenges posed by the energy transition. The focus topics involve an in-depth systemic and multidisciplinary knowledge of power converters and their components and applications.



Ralph Kennel (M'89-SM'96) received the Diploma and Dr. Ing. (Ph.D.) degrees in electrical engineering from the University of Kaiserslautern, Kaiserslautern, Germany, in 1979 and 1984, respectively.

From 1983 to 1999, he worked on several positions with Robert BOSCH GmbH (Germany). Until 1997, he was responsible for the development of servo drives. He was one of the main supporters of VECON and SERCOS interface, two multicompany development projects for a microcontroller and a digital interface especially dedicated to servo drives.

Furthermore, he actively took part in the definition and release of new standards with respect to CE marking for servo drives. Between 1997 and 1999, he was responsible for "Advanced and Product Development of Fractional Horsepower Motors" in automotive applications. His main activity was preparing the introduction of brushless drive concepts to the automotive market. From 1994 to 1999, he was appointed as a Visiting Professor with the Newcastle University, Newcastle-upon-Tyne, U.K. From 1999 to 2008, he was a Professor for electrical machines and drives with the Wuppertal University, Wuppertal, Germany. Since 2008, he has been a Professor for electrical drive systems and power electronics with Technische Universität München, Munich, Germany. His main interests include sensorless control of ac drives, predictive control of power electronics and hardware-in-the-loop systems.

Dr. Kennel is a fellow of IET (former IEE) and a Chartered Engineer in the U.K. Within IEEE, he is Treasurer of the Germany Section as well as Distinguished Lecturer of the Power Electronics Society (IEEE-PELS). He has received in 2013 the Harry Owen Distinguished Service Award from IEEE-PELS, the EPE Association Distinguished Service Award in 2015 as well as the 2019 EPE Outstanding Achievement Award. In 2018, he received the Doctoral degree honoris causa from Universitatea Stefan cel Mare in Suceava (Romania). He was appointed Extraordinary Professor by the University of Stellenbosch (South Africa) from 2016 to 2019 and as Visiting Professor with the Haixi Institute by the Chinese Academy of Sciences from 2016 to 2021.